OPEN ACCESS Freely available online

ISSN 2737-5323
Volume 3, Issue 1
https://www.iikii.com.sg/journal/AFM
Applied Functional Materials

Article

Platinum Nanotubes Calculated Using Relativistic Cylindrical Wave Technique: Chiral Induced Spin Selectivity

Pavel D'yachkov * , and Evgeny D'yachkov

Kurnakov Institute of General and Inorganic Chemistry of the Russian Academy of Sciences, Leninskii pr. 31, 119991 Moscow, Russia;
* Correspondence: p_dyachkov@rambler.ru, telephone +79032011976

Received: Jan 28, 2023; **Revised:** Feb 13, 2023;**Accepted:** Feb 28, 2023; **Published:** Mar 30, 2023

Abstract: Electronic and spin properties of chiral platinum nanotubes are calculated using the relativistic linear augmented cylindrical waves method. The spin-orbit coupling induces the strong splitting of nonrelativistic dispersion curves for the Fermi energy region. The large differences in spin densities of states for spins up and down can be used to create pure spin currents through the tubules. In the two series Pt (5, n_2) and Pt (10, n_2), the (5, 3) and (10, 7) nanotubes show the strongest chirality-induced spin selectivity effects.

Keywords: Platinum Nanotubes, Chirality, Cylindrical Waves, Spin-Orbit Interaction, Spin Currents

1. Introduction

Noble metals such as Pt, Au, Pd, and Ag nanotubes (NTs) show a variety of applications in nanoscale electronic and spintronic devices. Various techniques are developed to obtain such materials [1–7]. In particular, the single-walled Pt NTs can be obtained using an electron beam thinning of the platinum nanowires. The experimental studies show that the noble metal NTs have excellent electronic properties with ballistic quantum electron transport which finds practical applications [8-14]. Geometrically, the single-walled Pt NTs have the form of cylindrical surfaces covered with regular hexagons with one metal atom in the center of each hexagon (Fig. 1). It is convenient to represent their geometry as the result of rolling of platinum tapes into the cylinders. The Pt NTs can vary greatly in diameter and orientation of the hexagons relative to the z-axis.

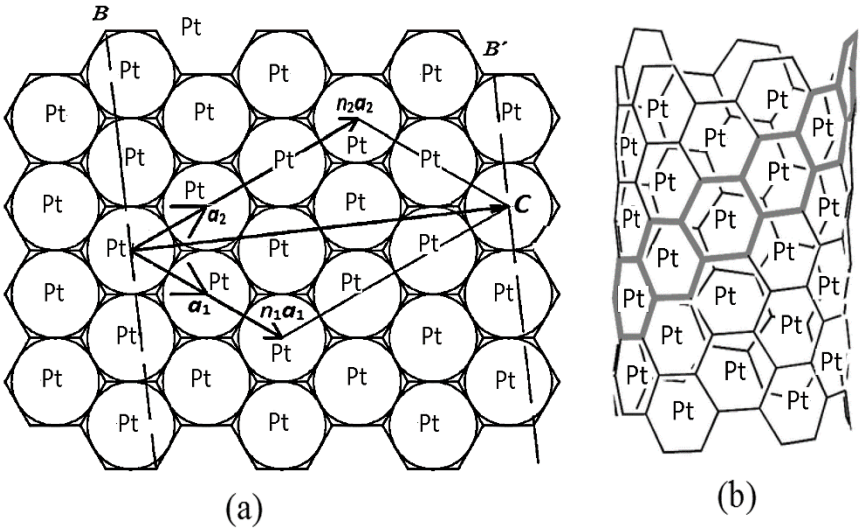

Fig. 1. Construction of the geometry of Pt NT (n_1, n_2) from the geometry of a monoatomic layer. Let us construct the vector $\mathbf{C} = n_1\mathbf{a}_1 + n_2\mathbf{a}_2$ on the monatomic platinum layer (a), then draw two straight lines B and B' perpendicular to this vector, cut out the strip bounded by these lines, and roll the strip into a cylinder (b) so that the lines B and B' coincide. The result is a tubule (n_1, n_2) with a diameter $d = C/\pi$.

The electronic properties of the Pt NTs differ sharply from similar properties of metallic platinum [15–18], since the Pt atoms in nanotubes are surrounded by the three neighboring atoms, while in the bulk Pt with a face-centered cubic lattice, by twelve atoms. In addition, the electronic properties of the Pt NTs depend on the fine details of their geometry such as the diameters, helicities, and chiralities, and a wide variety of NT structures leads to the great variations of their electronic properties. There are several calculations of the Pt NTs. In terms of the projector augmented plane wave method and density functional theory (DFT), the structure, stability, catalytic activity, and electronic dispersion curves of the two nonchiral Pt (6, 6) and (13, 13) NTs were calculated [19]. Using a similar approach, the electron and vibrational densities of states (DOS), and magnetic moments were calculated for the nonchiral clusters and the infinite length of Pt NTs consisting of the 5–8 Pt atoms coiling around the NTs axis [20]. The energetics and vibrational frequencies of the cylindrical multishell Pt structures were studied using a genetic algorithm [21]. Information on the electron DOS of only two helical Pt (6, 4) and (5, 3) NTs was obtained using cluster calculations and supercell models [22]. It is noted that the spin-orbit (SO) interactions were neglected in the calculations [19–22], but platinum is a heavy chemical element, and the SO coupling must be surely taken into account for its compounds. Our previous calculations of the two Pt NTs and a series of the Au NTs show that the SO coupling leads to the large band structure perturbation that appears as great electron band splitting and formation of the spin-dependent DOS and conductivity of the noble metal NTs [23,24]. The SO interaction manifests especially strongly in the case of NTs. Due to their cylindrical geometry, the electronic states of NTs correspond to the semi-classical electron rotations clockwise and anticlockwise around the tubules axis resulting in large orbital magnetic moments and SO coupling even for light element compounds such as the carbon or silicon NTs [25–29].

In recent years, the fundamental and applied aspects of the SO interaction in chiral one-dimensional systems have attracted great interest [30–39]. A fast-moving field of research called chiral spintronics is developing, when, unlike conventional electronics, the energy and information are transferred through a material not by electric curre1nt by the spin flows. A chemical compound is called chiral if it differs from its mirror image, as one of them has left-handed and the other right-handed helicity. In the one-dimensional helical chiral objects, the formation of spin currents is possible, and the moving spins become chiral too due to their mirror reflection asymmetry depending on the relative orientation of the spin and one-dimensional momentum k. The helical multiatomic systems coupled with moving spins and electrons with spins of certain handedness travel through chiral material with the same handedness in longer distances leading to spin-dependent currents. On the contrary, the difference between the helicities of the compound and electron spin reduces the electron mobility. The simplest explanation for this is that the probability $\tau_{\uparrow\uparrow}$ of electrons transmission/tunneling through the helical chiral potential barrier is greater when the barrier and spin helicities are parallel compared to the probability $\tau_{\uparrow\downarrow}$ when they are antiparallel ($\tau_{\uparrow\uparrow} > \tau_{\uparrow\downarrow}$) [40−50]. This effect, called chirality-induced spin selectivity (CISS), can be used for spin-dependent electron transfer and spin-filtering and recording and transmitting information in quantum computing [31−46]. The search for new materials for chiral spintronics seems to be an urgent task of nanomaterials science.

The purpose of this research is to study the spin and electronic properties of single-walled Pt NTs as promising materials for spintronics. To this end, the two series of helical chiral NTs were calculated using the symmetrized relativistic linear augmented cylindrical waves (LACW) method [28], namely, the NTs Pt (5, n_2) with $1 \le n_2 \le 4$ and (10, n_2) with $1 \le n_2 \le 9$ with radii between 2.24 and 7.78 Å. In previous work, the effects of the torsional, uniaxial, and uniform strains on the Pt (5, 5) and (5, 3) NTs were studied using this approach [24].

2. Method of Calculation

The LACW technique is an extension to the compounds with cylindrical geometry of the linear augmented plane waves method (LAPW), which is popular in the crystal's electron properties studies. The calculations are based on the two-component relativistic Hamiltonian as follows.

$$H = -\Delta + V(\mathbf{r}) + (1/c^2)\boldsymbol{\sigma}\cdot[(\nabla V(\mathbf{r})\times\mathbf{p}] \quad (1)$$

where the first two terms describe the nonrelativistic H_0 component of the Hamiltonian, and the third one is the SO coupling operator H_{S-O}. Rydberg atomic units are used, c is the speed of light, and σ is the Pauli matrices. For the potential $V(\mathbf{r})$, the muffin-tin (MT) and DFT approximations are used, which is popular in Slater's LAPW theory of bulk solids. Namely, for the electron potential $V(\mathbf{r})$ in the atomic region, its spherically symmetric part $V(r)$ is taken and the exchange interaction is calculated using the Slater $\rho^{1/3}$ potential. In the interatomic space, up to the internal and external impenetrable barriers, the potential is constant and is chosen as the origin of the energy. The nanotube electronic structures are determined by the free movement of electrons in the interspherical region by scattering of electrons at the atomic (MT) potentials and reflection from the two cylindrical barriers separating the nanotube's region from the outer and inner vacuum regions. The radii of MT spheres are equal to half of the Pt–Pt bond length d_{Pt-Pt} = 2.82 Å, and the distance between potential barriers 5.8 Å was chosen as the arithmetical mean of covalent and van der Waals diameters of the Pt atoms.

The geometry of the NTs is used as input information. It is defined by the interatomic distance $d_{Pt–Pt}$ and by the orientation of the hexagonal cells relative to the tubule axis and is usually described by the two integer indices (n_1, n_2), where $n_1 > 0$ and $0 \le n_2 \le n_1$. The (n_1, n_2) NTs have a rotational symmetry axis C_n, where n is the greatest common divisor of the n_1 and n_2, and, more importantly, a screw $S(h_z, \omega)$ symmetry. Here, $S(h_z, \omega)$ is the repeated operations of shifting

$$h_z = \frac{n\sqrt{3}d_{Pt-Pt}}{2\left(n_1^2 + n_2^2 + n_1 n_2\right)^{1/2}} \tag{2}$$

along the Z axis of the cylinder in combination with simultaneous rotations of

$$\omega = \pm 2\pi \frac{p_1 n_1 + p_1 n_1 + \left(p_2 n_1 + p_1 n_2\right)/2}{n_1^2 + n_2^2 + n_1 n_2} \tag{3}$$

about this axis. (The positive integers p_1 and p_2 are obtained from the equation $p_2 n_1 - p_1 n_2 = n$). The values of h_z and ω determine the helicity of the tubes. The positive and negative signs of the ω correspond to the tubules with the right-handed and left-handed chiralities.

The helical NTs have large translational unit cells. However, in the LACW method, taking into account the rotational C_n and screw $S(h_z, \omega)$ symmetries, it is possible to reduce the minimum cell of any Pt NT to only one atom, which makes it possible to apply the method to any NT regardless of its geometry. The symmetry properties are used in writing the basis functions and calculating the matrix elements of the Hamiltonian (Eq. (1)). We first calculate the eigenfunctions and eigenvalues of the H0, then we double the basis by including the spin functions and calculate the matrix elements of the $H_{S–O}$ as it is described in detail elsewhere [28]. As a result of calculations, the electronic eigenstates are determined by the electron spin and by the two quantum numbers, namely, the rotational quantum number $L = 0, 1, \ldots, n - 1$ and the wave vector $-\pi/h_z \le k \le \pi/h_z$ corresponding to helical translations.

3. Results and Discussions

Let's start the discussion with the results of calculations for right-handed helical nanotubes. Figures 2 and 3 show the band structures of such chiral Pt (5, n_2) and Pt (10, n_2) NTs. The band structures are given for positive values of the wave vectors k from the Brillouin zone center Γ ($k = 0$) to its edge K ($k = \pi/h_z$), since the dispersion curves are antisymmetric with respect to the replacement of k by $–k$.

$$E_\alpha(k, L) = E_\beta(-k, n - L) \tag{4}$$

That is, when the sign of the wave vector k changes, the electron energy is conserved, but the spin polarization is reversed. In the NTs with rotational axis C_n, the orbital quantum number L is to be replaced by $n – L$. The electron momenta for the states $E_\alpha(k, L)$ and $E_\beta(-k, n - L)$ coincide in absolute value but are oppositely directed as

$$dE_\alpha(k, L)/dk = -dE_\beta(-k, n - L)/dk. \tag{5}$$

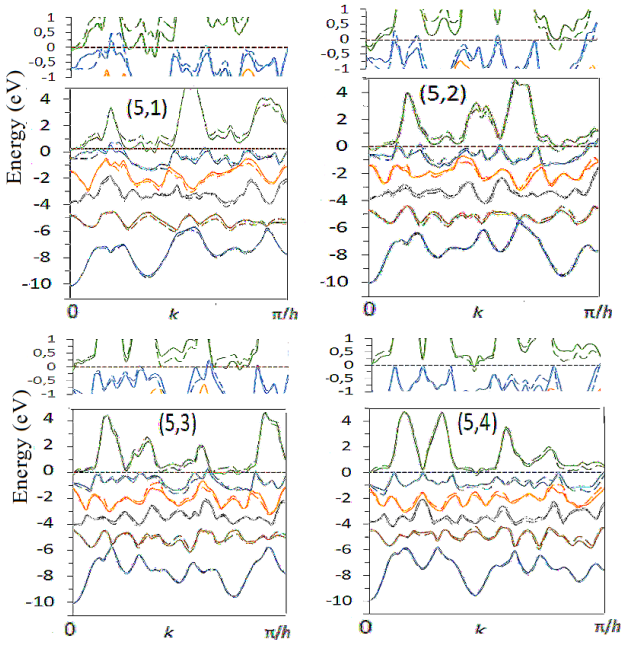

Fig. 2. Band structure of right-handed helical Pt (5, n_2) NTs. Here and below, the solid and dashed lines correspond to states with predominant α and β spins. In Fermi energy range, the dispersion curves are also shown on enlarged energy scale.

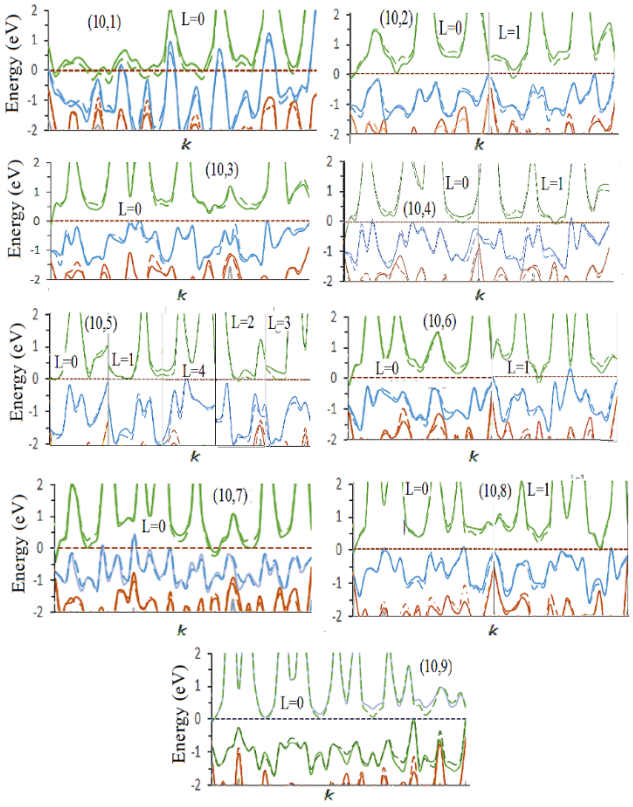

Fig. 3. Band structure of right-handed chiral Pt (10, n_2) NTs for Fermi energy region.

Figure 4 presents an example of band structure calculated for $-\pi/h_z \le k \le \pi/h_z$ and shows the band structures and DOS of the right-handed (5, 3) Pt NT calculated for $k \ge 0$ and $k \le 0$ and demonstrates the validity of Eqs. (4)-(6).

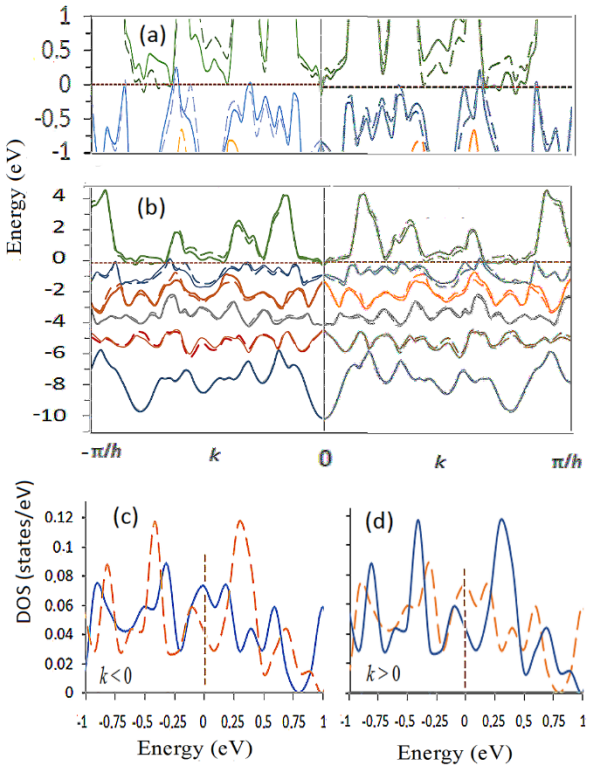

Fig. 4. Band structures (a), (b) and DOS (c), (d) of right-handed helical Pt NT (5, 3), presented for the total Brillouin zone region with wave vectors $k < 0$ and $k > 0$. The solid and dashed lines correspond to states with spins α and β.

With one atom per hexagonal cell of the tubules and the electronic configuration of the Pt atom $5d^9 6s^1$, the results can be presented in a simple form with the ten spin-dependent dispersion curves of the valence band, above which the conduction band states are located. The Fermi level separates the valence and conduction band dispersion curves. The boundary curves of these bands do not intersect, but the valence band top and the conduction band bottom overlap with the Fermi level. The SO coupling manifests itself as the strong splitting of nonrelativistic dispersion curves, which exceeds 0.5 eV for bands of the Fermi region. The predominant spin polarizations for the split pairs of bands are opposite. For the $k > 0$, the spin up (α) corresponds to the case when the helicities of the right-handed nanotube and spin coincide, and spin down (β), when they are opposite. Upon a transition to the internal states of the valence band, the SO splitting of the bands weakens to about 0.1 eV. In the (10, n_2) NTs, the SO splitting is somewhat smaller. With increasing the n_2 index and, as a consequence, the diameter of tubules, the band's SO splitting decreases too. Let us note that these results for the Pt NTs are in reasonable agreement with the band structure of crystalline platinum obtained using the similar relativistic LAPW method with the MT approximation [15]. In particular, the valence bandwidth in both the crystal and NTs is equal to 10 eV, and the energies of the SO splitting of the dispersion curves near the Fermi level for high symmetry points of the Brillouin zone in the crystal are equal to the 0.35–1.1 eV. According to previous *ab initio* calculations, the bulk Pt, its low-index surfaces, and the nonchiral Pt NTs are all zero-gap materials too [15−22].

For the right-handed chiral Pt NTs, Figs. 5 and 6 show the spin-dependent DOS in the vicinity of Fermi level for electrons with spin up $N(\alpha)|_{k>0}$ and spin down $N(\beta)|_{k>0}$ for the case of positive values of the wave vector $k > 0$ corresponding to the electron flow in the positive direction of the z-axis. For opposite direction, the $N(\alpha)|_{k<0}$ and $N(\beta)|_{k<0}$ are found from the relations

$$N(\alpha)|_{k<0} = N(\beta)|_{k>0},\ N(\beta)|_{k<0} = N(\alpha)|_{k>0} \quad (6)$$

according to which the DOS does not change with a simultaneous reversal in the direction of motion of electrons and their spins. Figure 4 clearly illustrates the validity of these relations.

The $N_F(\alpha)|_{k>0}$ and $N_F(\beta)|_{k>0}$ values at the Fermi level are different that can be used to create the spin filters and purely spin currents through the tubules, which are understood as the electron flows with the finite spin polarization, but zero transferred charge [36, 40]. The NTs with higher total DOS at the Fermi level

$$N_F = N_F(\alpha)|_{k>0} + N_F(\beta)|_{k>0} \quad (7)$$

and with greater positive spin polarizability

$$P_F = (1/N_F)[N_F(\alpha)|_{k>0} - N_F(\beta)|_{k>0}] \quad (8)$$

are more suitable for this.

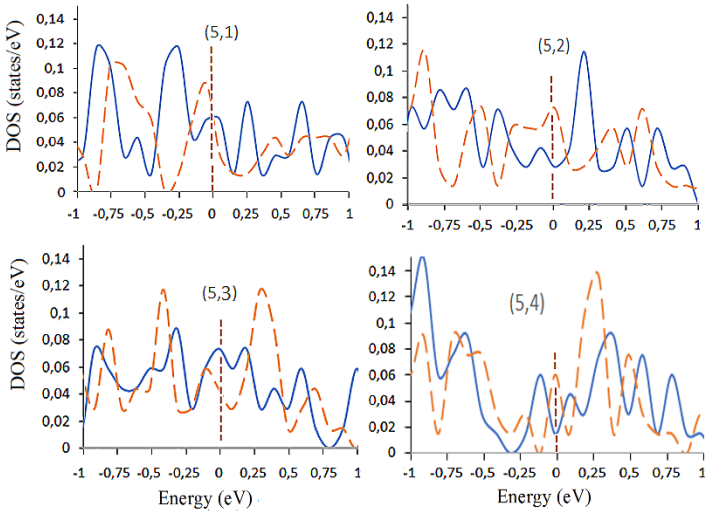

Fig. 5. Densities of spin states $N(\alpha)|_{k>0}$ and $N(\beta)|_{k>0}$ for spins up and down calculated per atom for right-handed helical Pt (5, n_2) NTs.

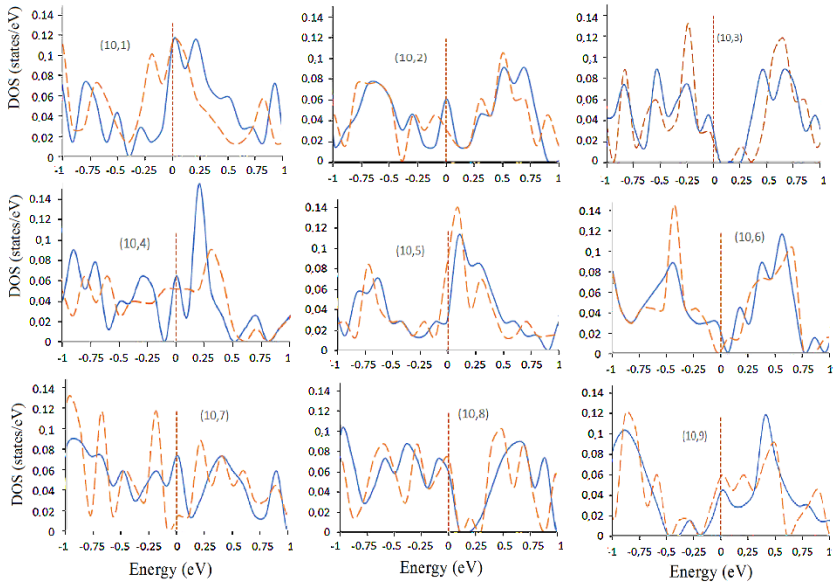

Fig. 6. Densities of spin states for right-handed chiral Pt (10, n_2) NTs.

In the Pt (5, n_2) series, only one, namely, the (5, 3) NT with the parameters $N_F(\alpha)|_{k>0} = 0.075$, $N_F(\beta)|_{k>0} = 0.04$, $N_F = 0.115$ states/eV, and $P_F = 0.3$ satisfy these conditions (Table 1). In this case, for the positive direction of the axis $z > 0$, the concentration of mobile electrons with spin α is almost two times higher than with spin β, and according to Eq. (6) for the opposite direction $z < 0$, the concentration of mobile electrons with spin β is the same times greater than with spin α. The spin currents in the $z > 0$ direction for the electrons with spins α and β are proportional to the product of concentrations of electrons with given spin at the Fermi level and to the probabilities of electron tunneling/transmission through chiral potential barriers $I(\alpha)_{z>0} \sim \tau_{\uparrow\uparrow} N(\alpha)|_{k>0}$ and $I(\beta)_{z>0} \sim$

$\tau_{\uparrow\downarrow}N(\beta)|_{k>0}$ (the helicities of the tubule and α spin are parallel, and for β spins they are antiparallel). Since $N(\alpha)|_{k>0} > N(\beta)|_{k>0}$ and $\tau_{\uparrow\uparrow} > \tau_{\uparrow\downarrow}$, we have $I(\alpha)_{z>0} > I(\beta)_{z>0}$, that is, for the direction $z > 0$ of the Pt (5, 3) NT the flow of electrons with spin α will be greater than with spin β. For the opposite $z < 0$ direction, the helicities of the barrier and of the β spin coincide, so so $I(\beta)_{z<0} \sim \tau_{\uparrow\uparrow}N(\beta)|_{k<0}$ and $I(\alpha)_{z<0} \sim \tau_{\uparrow\downarrow}N(\alpha)|_{k<0}$. According to Eq. (6), the $N(\beta)|_{k<0} > N(\alpha)|_{k<0}$, and hence the $I(\beta)_{z<0} > I(\alpha)_{z<0}$; the transport of β electrons will prevail over that of the α electrons.

Table 1. Spin DOS, total DOS, and spin polarizability of states at the Fermi level for the right-handed chiral Pt NTs.

Pt NTs	$N_F(\alpha)\|_{k>0}$, states/eV	$N_F(\beta)\|_{k>0}$, states/eV	N_F, states/eV	P_F
(5, n_2) Pt				
(5, 1)	0.06	0.07	0.13	–0.08
(5, 2)	0.025	0.07	0.095	–0.05
(5, 3)	0.075	0.04	0.115	0.30
(5, 4)	0.015	0.06	0.075	–0.60
(10, n_2) Pt				
(10, 1)	0.11	0.11	0.22	0
(10, 2)	0.06	0.03	0.09	0.33
(10, 3)	0.03	0.02	0.05	0.20
(10, 4)	0.06	0.05	0.11	0.09
(10, 5)	0.04	0.09	0.13	–0.38
(10, 6)	0.02	0.00	0.02	1.0
(10, 7)	0.07	0.01	0.08	0.75
(10, 8)	0.06	0.07	0.13	–0.08
(10, 9)	0.045	0.06	0.105	–0.14

These features of the electronic structure of chiral Pt NTs can be used to create pure spin currents. For example, if now this NT is placed between the two contacts and an alternating voltage U is applied so that under the action of an electric field during the time t from zero to T the electrons move in the z direction, and then for the time between T and 2T the voltage is replaced by the opposite $–U$, then there will be zero total charge transfer in the system over time $2T$ [33]. However, during the first time interval, mainly the electrons with α spin will move in the z direction, and during the second interval, the electrons with β spin in the $–z$ direction [33]. Thus, with the help of an alternating electric field, it is possible to carry out the transport of electrons with different spins in opposite directions without the total charge transfer.

In the (5, 1), (5, 2), and (5, 4) NTs, the $N_F(\beta)|_{k>0} > N_F(\alpha)|_{k>0}$, that is, the concentration of mobile electrons with spin β is larger than with spin α for the positive z direction. On the other hand, for $z > 0$, the probability of electrons passing through the chiral barrier is greater for α spins ($\tau_{\uparrow\uparrow}$) than for β spins ($\tau_{\uparrow\downarrow}$). These two factors (the concentrations of mobile electrons with different spins and the probabilities of their passage through the helical potential barriers) have the opposite effects on the magnitudes of the spin currents $I(\beta)$ and $I(\alpha)$ for both positive and negative directions of the z-axis preventing the creation of large spin flows. Therefore, these NTs are less suitable for generating spin currents compared to the Pt (5, 3) NT.

For the (10, n_2) NTs, similar arguments together with the data in Table 1 indicate that the (10, 6) and (10, 7) NTs with the large positive values of the spin polarizability at the Fermi level $P_F = 1$ and 0.75 are the most suitable for creating the large spin currents. However, for the (10, 6) NT, the total DOS at the Fermi level $N_F = 0.02$ states/eV is the lowest in the entire series of compounds, and in the (10, 7) tubule $N_F = 0.08$ states/eV. Therefore, with the large $N_F(\alpha)|_{k>0} = 0.07$ states/eV, small $N_F(\beta)|_{k>0} = 0.01$ states/eV, and the large N_F and P_F values, one can expect the strongest spin transport effect in the (10, 7) NT. For the NTs (10, 1), (10, 2), (10, 3), and (10, 4) of series (10, n_2), the main requirement $N_F(\alpha)|_{k>0} > N_F(\beta)|_{k>0}$ is also met, and for the final choice between these NTs, it is necessary to know the numerical values of the transmission coefficients $\tau_{\uparrow\uparrow}$ and $\tau_{\uparrow\downarrow}$ that, however, is beyond the scope of band structure technique [40]. The results of calculations of the electronic structures of right-handed nanotubes are easily converted into the band structures and DOS of the left-handed analogs. To do this, it is enough to interchange the solid and dashed lines in Figs.

5−6 as it is shown in Fig. 7 for the band structures of the right-handed and left-handed helical (10, 4) NTs. In particular, it follows from here that in the positive direction of the z-axis, the electron transport with spins β will dominate compared to α spins for the left-handed (5, 3) and (10, 7) nanotubes.

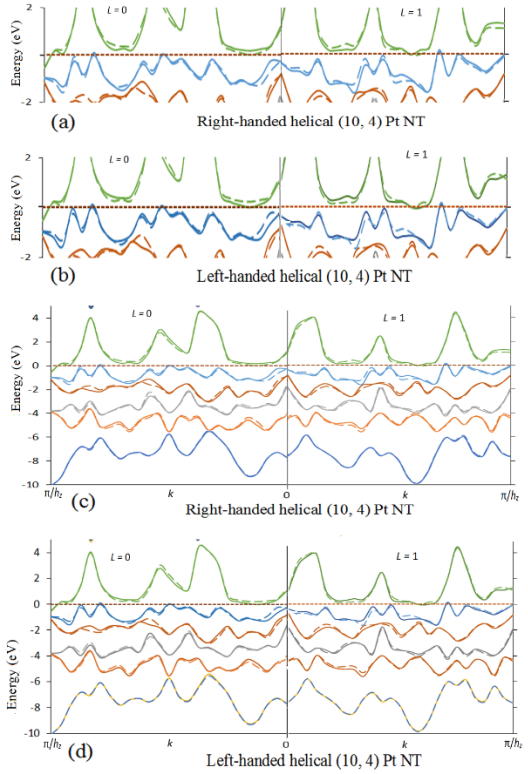

Fig. 7. Band structures of right-handed (a), (c) and left-handed (b), (d) helical (10, 4) Pt NTs.

Supplementary File: It is available online at www.iikii.com/afm/xxx/s001. Here, the band structures and DOS of the right- and left-handed helical chiral Pt (5, 3) and (10, 4) NTs are presented for $-\pi/h_z \leq k \leq \pi/h_z$.

Author Contributions: All authors contributed equally to this work.

Funding: This research was funded by the Russian Science Foundation Grant No. 22-23-00154, https:rscf.ru/project/22-23-00154/.

Conflicts of Interest: The authors declare no conflict of interest.

References

1. Oshima, Y.; Koizumi, H.; Mouri, K.; Hirayama, H.; Takayanagi, K.; Kondo, Y. Evidence of a single-wall platinum nanotube. *Phys. Rev. B*. **2002,** *65*, 121401(R). https://doi.org/10.1103/PhysRevB.65.121401
2. Oshima, Y.; Onga, A.; Takayanagi, K. Helical gold nanotube synthesized at 150 K. *Phys. Rev. Lett.* **2003,** *91*, 205503. https://doi.org/10.1103/PhysRevLett.91.205503
3. Huang, Z.; Raciti, D.; Yu, S.; Zhang, L.; Deng, L.; He, J.; Liu, Y., Khasha, N.M.; Wang, C.; Gong, J.; Nie, Z. Synthesis of platinum nanotubes and nanorings via simultaneous metal alloying and etching. *J. Am. Chem. Soc.* **2016**, *138*, 6332–6335. https://doi.org/10.1021/jacs.6b01328
4. Bi, Y.; Lu, G. Control growth of uniform platinum nanotubes and their catalytic properties for methanol electrooxidation. Electrochem. Commun. **2009,** *11*, 45–49. https://doi.org/10.1016/j.elecom.2008.10.023
5. Lou, X.W.; Archer, L.A.; Yang, Z. Hollow micro-/nanostructures: synthesis and applications. *Adv. Mater*. **2008,** *20*, 3987–4019. https://doi.org/10.1002/adma.200800854
6. Zhang, G.; Sun, S.; Cai, M.; Zhang, Y.; Li, R.; Sun, X. Porous dendritic platinum nanotubes with extremely high activity and stability for oxygen reduction reaction. *Scientific. Rep*. **2013,** *3*, 1526. https://doi.org/10.1038/srep01526
7. Hendren, W.R.; Murphy, A.; Evans, P.; O'Connor1, D.; Wurtz, G.A.; Zayats, A.V.; Atkinson, R.; Pollard, R.J. Fabrication and optical properties of gold nanotube arrays. *J. Phys.: Condens. Matter*. **2008,** *20*, 362203. https://doi.org/10.1088/0953-8984/20/36/362203

8. Oshima, Y.; Mouri, K.; Hirayama, H.; Takayanagi K. Quantized electrical conductance of gold helical multishell nanowires. *J. Phys. Soc. Jpn*. **2006,** *75*, 053705. https://doi.org/10.1143/jpsj.75.053705
9. Del Valle, M.; Tejedor, C.; Cuniberti, G. Scaling of the conductance in gold nanotubes. *Phys. Rev. B.* **2006,** *74*, 045408. https://doi.org/10.1103/PhysRevB.74.045408
10. Rajala, T.; Kronberga, R.; Backhouse, R. A platinum nanowire electrocatalyst on single-walled carbon nanotubes to drive hydrogen evolution. *Appl. Catal. B: Environmental*. **2020,** *265*, 118582. https://doi.org/10.1016/j.apcatb.2019.118582
11. Ono, T.; Hirose, K. First-principles study of electron-conduction properties of helical gold nanowires. *Phys. Rev. Lett*. **2005,** *94*, 206806. https://doi.org/10.1103/PhysRevLett.94.206806
12. Zhang, K.; Zhang, H. Plasmon coupling in gold nanotube assemblies: insight from a time-dependent density functional theory (tddft) calculation. *J. Phys. Chem. C.* **2014,** *118*, 635–641. https://doi.org/10.1021/jp410056u
13. Kumar, J.; Thomas, K.G.; Liz-Marzán, L.M. Nanoscale chirality in metal and semiconductor nanoparticles. *Chem. Commun.* **2016,** *52*, 12555 -12569. https://doi.org/10.1039/C6CC05613J
14. Manrique, D.Zs. J. Cserti, C.J. Lambert. Chiral currents in gold nanotubes. *Phys. Rev. B.* **2010,** *81*, 073103. https://doi.org/10.1103/PhysRevB.81.073103
15. Andersen, O.K. Electronic structure of the fcc transition metals Ir, Rh, Pt, and Pd. *Phys. Rev. B.* **1970,** *2*, 883–907. https://doi.org/10.1103/PhysRevB.2.883
16. Leschik, G., Courths, R.; Wern, H.; Hiifner, S.; Eckardt, H.; Noffke, J. Band structure of platinum from angle resolved photoemission experiments. *Solid State Commun*. **1984,** *52* (2), 221-225. https://doi.org/10.1016/0038-1098(84)90631-8
17. Herrera-Suárez, H.J.; Rubio-Ponce, A.; Olguín, D. Empirical electronic band structure study of silver low-index surfaces. *Mexicana de Física.* **2012,** *58*, 46–54. https://doi.org/10.48550/arXiv.1311.5929
18. Wern, H.; Courths, R.; Leschik, G.; Hufner, S. On the band structure of silver and platinum from angle-resolved photoelectron spectroscopy (ARUPS) measurements. *Z. Physics B: Condensed Matter*. **1985,** *60*, 293–310. https://doi.org/10.1007/BF01304449
19. Matanović, I.; Kent, P.R.C.; Garzon, F.H.; Henson, N.J. Density Functional Study of the Structure, Stability and Oxygen Reduction Activity of Ultrathin Platinum Nanowires. *J. Electrochem. Soc*. **2013,** *160*, F548–F553. https://doi.org/10.1149/2.047306jes
20. Xiao, L.; Wang, L. Density functional theory study of single-wall platinum nanotubes. *Chem. Phys. Lett*. **2006,** *430*, 319–322. https://doi.org/10.1016/j.cplett.2006.09.032
21. Hui, L.; Pederiva, F.; Guanghou, W.; Baolin, W. Structural calculation and properties of one-dimensional Pt materials. *Chem. Phys. Lett*. **2003,** *381*, 94–101 (). https://10.1016/j.cplett.2003.08.110
22. Konar, S.; Gupta, B.C. Density functional study of single-wall and double-wall platinum nanotubes. *Phys. Rev. B.* **2008,** *78*, 235414. https://doi.org/10.1103/PhysRevB.78.235414
23. D'yachkov, E.P.; D'yachkov, P.N. Gold nanosolenoids based on chiral nanotubes calculated using the relativistic linearized augmented cylindrical wave method. *J. Phys. Chem. C.* **2019,** *123*, 26005-26010. https://doi.org/10.1021/acs.jpcc.9b07610
24. D'yachkov, P.N.; Krasnov, D.O. Electronic and transport properties of deformed platinum nanotubes calculated using relativistic linear augmented cylindrical wave method. *Chem. Phys. Lett*. **2019,** *720*, 15-18. https://doi.org/10.1016/j.cplett.2019.02.006
25. Ando, T. Theory of electronic states and transport in carbon nanotubes. *J. Phys. Soc. Jpn*. **2000,** *69*, 1757–1763. https://doi.org/10.1143/JPSJ.74.777
26. Minot, E.D., Yaish, Y.; Sazonova, V.; McEuen, P.L. Determination of electron orbital magnetic moments in carbon nanotubes. *Nature* **2004,** *428*, 536–539. https://10.1038/nature02425
27. Kuemmeth, F.; Ilani, S.; Ralph, D.C.; McEuen, P.L. Coupling of spin and orbital motion of electrons in carbon nanotubes. *Nature* **2008,** *452*, 448–452. https://10.1038/nature06822
28. D'yachkov, P.N. *Quantum chemistry of nanotubes: electronic cylindrical waves*. **2019**, CRC Press. London: Taylor and Francis, 212 p.
29. D'yachkov, P.N.; D'yachkov, E.P. Rashba spin–orbit interaction effect in twisted silicon nanotubes for chiral spintronics. *Appl. Phys. Lett.* **2022,** *120*, 173101. https://doi.org/10.1063/5.0086902
30. Yang, S.H. Spin-orbit torques: Materials, physics, and devices. *Appl. Phys. Lett*. **2021,** *16*, 120502. https://doi.org/10.1063/5.0039147
31. Yang, S.H.; Naaman, R.; Paltiel, Y.; Parkin, S.S.P. Chiral spintronics. *Nature Rev. Phys*. **2021,** *3*, 328-343. https://doi.org/10.1038/s42254-021-00302-9
32. Michaeli, K.; Kantor-Uriel, N.; Naamanm, R.; Waldeck, D.H. The electron's spin and molecular chirality – how are they related and how do they affect life processes? *Chem. Soc. Rev*. **2016,** *45*, 6478. https://doi.org/10.1039/C6CS00369A
33. Bercioux, D.; Lucignano, P. Quantum transport in Rashba spin–orbit materials: a review. *Rep. Prog. Phys.* **2015,** *78*, 106001. https://doi.org/10.1088/0034-4885/78/10/106001
34. Naaman, R.; Waldeck, D.H. Spintronics and chirality: spin selectivity in electron transport through chiral molecules. *Annu. Rev. Phys. Chem*. **2015,** *66*, 263–281. https://doi.org/10.1146/annurev-physchem-040214-121554

35. Banerjee-Ghosh, K.; Dor, O.B.; Tassinari, F.; Capua, E.; Yochelis, S.; Capua, A.; Yang, S.-H.; Parkin, S.S.P.; Sarkar, S.; Kronik, L.; Baczewski, L.T.; Naaman, R.; Paltiel, Y. Separation of enantiomers by their enantiospecific interaction with achiral magnetic substrates. *Science* **2018,** *360*, 1331–1334. https://doi.org/10.1126/science.aar4265
36. Manchon, A.; Koo, H.C.; Nitta, J.; Frolov, S. M.; Duine, R.A. New perspectives for Rashba spin–orbit coupling. *Nature Mater*. **2015,** *14*, 871-882. https://doi.org/10.1038/nmat4360
37. Waldeck, D.H.; Naaman, R.; Paltiel, Y. The spin selectivity effect in chiral materials. *APL Mater.* **2021,** *9*, 040902. https://doi.org/10.1063/5.0049150
38. Yeom. J. Atomic chirality and a materials revolution. *Acc. Mater. Res*. **2021,** *2* (7), 471–476. https://doi.org/10.1021/accountsmr.1c00059
39. Yang, X.; van der Wal, C.H.; van Wees, B.J. Detecting chirality in two-terminal electronic nanodevices. *Nano Lett*. **2020,** *20* (8), 6148–6154. https://doi.org/10.1021/acs.nanolett.0c02417
40. Yeganeh, S.; Ratner, M.A.; Medina, E.; Mujica, V.. Chiral electron transport: scattering through helical potentials. *J. Chem. Phys.* **2009,** *131*, 014707. https://doi.org/10.1063/1.3167404
41. Gutierrez, R.; Díaz, E.; Naaman, R.; Cuniberti, G. Spin-selective transport through helical molecular systems. *Phys. Rev. B* **2012,** *85*, 081404(R). ttps://doi.org/10.1103/PhysRevB.85.081404
42. Gutierrez, R.; Díaz, E.; Gaul, C.; Brumme, T.; Domínguez-Adame, F.; Cuniberti, G. Modeling spin transport in helical fields: derivation of an effective low-dimensional Hamiltonian. *J. Phys. Chem. C*. **2013,** *117*, 22276–22284.
43. Eremko, A.A.; Loktev, V.M. Spin sensitive electron transmission through helical potentials. *Phys. Rev. B* **2013,** *88*, 165409. https://doi.org/10.1103/PhysRevB.88.165409
44. Yang, X.; van der Wal, C.H.; van Wees, B.J. Spin-dependent electron transmission model for chiral molecules in mesoscopic devices. *Phys. Rev. B* **2019,** *99*, 024418. https://doi.org/10.1103/PhysRevB.99.024418
45. Dalum, S.; Hedegård, P. Theory of chiral induced spin selectivity. *Nano Lett.* **2019,** *19* (8), 5253–5259. https://doi.org/10.1021/acs.nanolett.9b01707
46. Rahman, W.; Firouzeh, S.; Mujica, V.; Pramanik, S. Carrier transport engineering in carbon nanotubes by chirality-induced spin polarization. *ACS Nano* **2020,** *14*, 3389−3396. https://doi.org/10.1021/acsnano.9b09267
47. Ghazaryan, A.; Paltiel, Y.; Lemeshko, M. Analytic model of chiral-induced spin selectivity. *J. Phys. Chem. C* **2020,** *124*, 11716−11721. https://doi.org/10.1021/acs.jpcc.0c02584
48. Zöllner, M.S.; Nasri, R.; Zhang, H.; Herrmann, C. Design considerations for oligo(p-phenyleneethynylene) organic radicals in molecular junctions. *J. Phys. Chem. C* **2021,** *125*, 1208-1220. https://doi.org/10.1021/acs.jpcc.0c08957
49. Michaeli, K.; Naaman, R. Origin of spin-dependent tunneling through chiral molecules. *J. Phys. Chem. C* **2019,** *123*, 17043-17048. https://doi.org/10.1021/acs.jpcc.9b05020
50. Naaman, R.; Paltiel, Y.; Waldeck, D.H. Chiral molecules and the spin selectivity effect. *J. Phys. Chem. Lett*. **2020,** *11*, 3660−3666. https://doi.org/10.1021/acs.jpclett.0c00474

Publisher's Note: IIKII stays neutral with regard to jurisdictional claims in published maps and institutional affiliations.